PNAS RESEARCH ARTICLE | CELL BIOLOGY
BIOPHYSICS AND COMPUTATIONAL BIOLOGY

OPEN ACCESS

Myosin turnover controls actomyosin contractile instability

Sathish Thiyagarajan[a,b], Shuyuan Wang[a], Ting Gang Chew[c], Junqi Huang[c], Lokesh Kumar[c], Mohan K. Balasubramanian[c], and Ben O'Shaughnessy[b,1]

Edited by David Weitz, Harvard University, Cambridge, MA; received July 11, 2022; accepted August 23, 2022

Actomyosin contractile force produced by myosin II molecules that bind and pull actin filaments is harnessed for diverse functions, from cell division by the cytokinetic contractile ring to morphogenesis driven by supracellular actomyosin networks during development. However, actomyosin contractility is intrinsically unstable to self-reinforcing spatial variations that may destroy the actomyosin architecture if unopposed. How cells control this threat is not established, and while large myosin fluctuations and punctateness are widely reported, the full course of the instability in cells has not been observed. Here, we observed the instability run its full course in isolated cytokinetic contractile rings in cell ghosts where component turnover processes are absent. Unprotected by turnover, myosin II merged hierarchically into aggregates with increasing amounts of myosin and increasing separation, up to a maximum separation. Molecularly explicit simulations reproduced the hierarchical aggregation which precipitated tension loss and ring fracture and identified the maximum separation as the length of actin filaments mediating mechanical communication between aggregates. In the final simulated dead-end state, aggregates were morphologically quiescent, including asters with polarity-sorted actin, similar to the dead-end state observed in actomyosin systems in vitro. Our results suggest the myosin II turnover time controls actomyosin contractile instability in normal cells, long enough for aggregation to build robust aggregates but sufficiently short to intercept catastrophic hierarchical aggregation and fracture.

myosin | actomyosin | aggregation | cytokinesis | turnover

Many fundamental single-cell and tissue-level processes rely on force production by actomyosin assemblies. During cytokinesis the actomyosin contractile ring develops tension that guides or drives furrow ingression and physical division of the cell (1–3). Tension gradients in the actomyosin cortex produce cortical flows that establish cell polarity (4) and cortical actomyosin forces are harnessed for cell migration (5). Contraction of supracellular actomyosin networks drives early tissue morphogenetic events such as gastrulation (6, 7) and neurulation in vertebrates (8).

In these systems, actomyosin contractility finds use as a powerful and highly adaptable tool, in which contractile stress generated by constrained myosin II molecules that bind and exert force on oriented filamentous actin is harnessed for diverse functions. However, the mechanism has an intrinsic instability. A chance fluctuation in the density of myosin II and other components may enhance local contractile stress and draw in more actomyosin material at the expense of weaker neighboring regions, further amplifying the stress difference in a potentially runaway aggregation process (Fig. 1*A*). Unchecked, catastrophic fracture and tension loss may result.

How the cytokinetic contractile ring and other actomyosin machineries deal with this threat is not established. Some examples of the instability have been documented. In cells, actomyosin stress fibers spontaneously sever or undergo repair in regions of high strain (9, 10), and in vitro myosin II spontaneously aggregated into puncta in reconstituted actomyosin bundles (11). Theoretical evidence for contractile instability is abundant, as in molecularly explicit (12) and continuum (13, 14) mathematical models of the fission yeast contractile ring and continuum models of the animal cell cortex (15, 16).

Observing actomyosin contractile instability run its full course in cells has proved challenging, presumably because mechanisms intervene before its full maturation. Nevertheless, numerous observations are suggestive of incipient instability. Large fluctuations and punctateness characterize myosin II distributions in fission yeast and animal cell contractile rings (17, 18) and animal cell cortices (19, 20). Punctate cortical myosin in some cases has pulsatile time dependence over seconds to minutes (21), which may be associated with pulsatile dynamics of the GTPase RhoA that promotes myosin II activity and minifilament assembly (4, 16, 22). Many morphogenetic events feature

Significance

Contractile force produced by myosin II that binds and pulls constrained filamentous actin is harnessed by cells for diverse processes such as cell division. However, contractile actomyosin systems are vulnerable to an intrinsic aggregation instability that destroys actomyosin architecture if unchecked. Punctate myosin distributions are widely observed, but how cells prevent more advanced aggregation remains unclear. Here, we studied cytokinetic contractile rings in fission yeast cell ghosts lacking component turnover, when myosin aggregated hierarchically. Simulations reproduced the severe organizational disruption and a dead-end state with isolated aggregates and ring tension loss. We conclude that in normal cells, myosin turnover regulates actomyosin contractile instability by continuous injection of homogeneously distributed myosin, permitting functional aggregates to develop but intercepting catastrophic runaway aggregation.

Author affiliations: [a]Department of Physics, Columbia University, New York, NY 10027; [b]Department of Chemical Engineering, Columbia University, New York, NY 10027; and [c]Warwick Medical School, University of Warwick, Coventry CV4 7AL, United Kingdom

---

Author contributions: M.K.B. and B.O. designed research; S.T., S.W., T.G.C., J.H., L.K., M.K.B., and B.O. performed research; S.T. and S.W. contributed new analytic tools; S.T., S.W., L.K., M.K.B., and B.O. analyzed data; and S.T., S.W., and B.O. wrote the paper with input from all authors.

The authors declare no competing interest.

This article is a PNAS Direct Submission.

[1]To whom correspondence may be addressed. Email: bo8@columbia.edu.

This article contains supporting information online at http://www.pnas.org/lookup/suppl/doi:10.1073/pnas.2211431119/-/DCSupplemental.

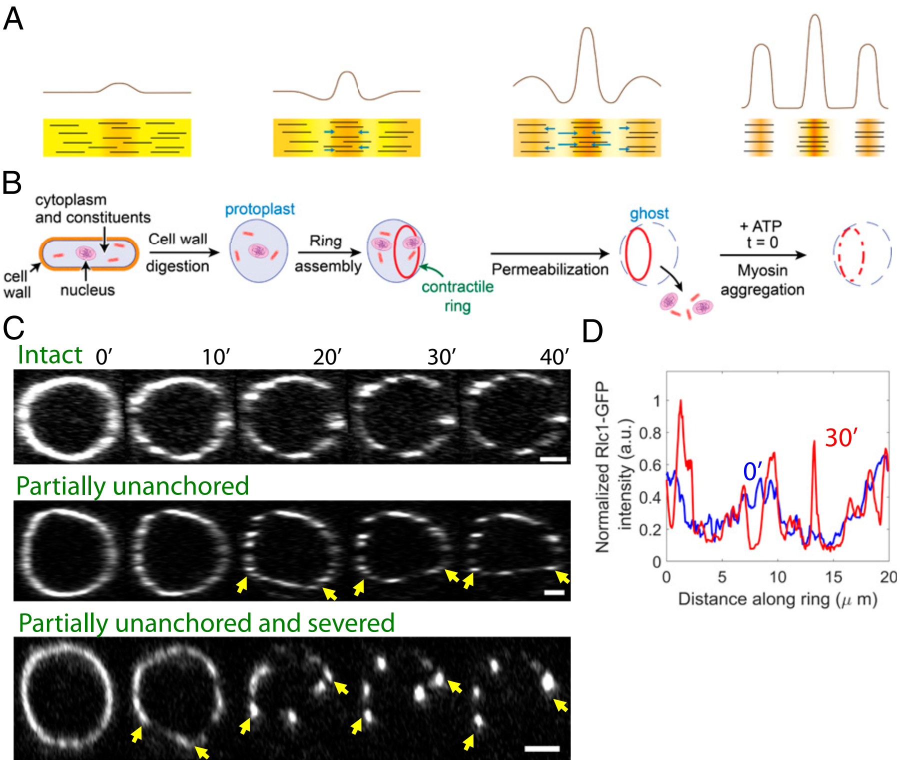

Fig. 1. Aggregation of myosin II in contractile rings of cell ghosts. (*A*) Actomyosin contractile instability, schematic. A fluctuation in the local density of contractile actomyosin material (*Left*) generates contractile stress gradients and flows (arrows) that pull material inward and amplify the fluctuation. Unopposed, the result is runaway aggregation and fracture (*Right*). Yellow/orange/brown background and black lines symbolically represent myosin density and actin filaments, respectively. Density profiles are shown above schematics of the actomyosin material. (*B*) Preparation of cell ghosts. Following enzymatic digestion of cell walls of normal cells of the fission yeast *S. japonicus*, the plasma membrane is permeabilized to release cytoplasm. In cells which have assembled cytokinetic rings, the rings remain anchored to the membrane. On addition of ATP, myosin II in rings aggregates progressively. (*C*) Time-lapse fluorescence micrographs of *S. japonicus* cell ghosts labeled with Rlc1-GFP following addition of 0.5 mM ATP. Images are sum-intensity projections of 3D reconstructions of rings from z-series data. Imaging commenced at least 1 to 2 min after ATP addition (see *Methods*). Contractile rings remain fully anchored to the membrane (*Top*), or ring segments appear to detach from the membrane and shorten (*Middle*), or segments detach, shorten, and sever (*Bottom*). Arrows indicate detached segments. We observed n = 6, 5, and 16 rings in each category, respectively. (Scale bars, 2 μm.) (*D*) Rlc1-GFP intensity along the ring at the indicated times for the intact ring of *C*. Intensity normalized by the total intensity around the ring at each time. (See *SI Appendix*, Fig. S1*A* for the intensity profiles around the partially unanchored and the partially unanchored and severed ring, respectively.)

pulsed actomyosin epithelial contractions with punctate myosin II distributions (6, 23).

Several candidate mechanisms that could control actomyosin contractile instability have been proposed. One possibility is turnover of myosin and actin (24, 25), which presumably tends to homogenize spatial variations (12). Another suggestion is myosin II diffusivity, which could serve this purpose by smoothing small-scale density variations characteristic of the instability (15, 26). Another proposal, suggested for *C. elegans* zygotes, is that the instabilities are controlled by pulsatile RhoA dynamics (16).

Here we examined the role of component turnover as a possible regulator of actomyosin contractile instability by studying cytokinetic contractile rings in cell ghosts under conditions where turnover is absent (27, 28). We find runaway aggregation of myosin II, in which the amount of myosin per aggregate and the separation between aggregates increases with time, up to a certain maximum separation. The aggregation is hierarchical, with repeated rounds of aggregation yielding aggregates with yet more myosin. In molecularly explicit simulations the maximum separation was identified as the length of actin filaments which mediate mechanical communication between aggregates, and small-scale instability was controlled not by myosin diffusivity but by local excluded volume and actin filament polarity sorting effects. Our results suggest that in normal cells myosin II turnover controls contractile instability in actomyosin assemblies, setting the size of myosin II aggregates and preventing catastrophic hierarchical aggregation and fracture.

Results

Component Turnover Is Absent in Contractile Rings of Cell Ghosts of the Fission Yeast *Schizosaccharomyces japonicus*. To investigate whether component turnover plays a role in maintaining organization in the cytokinetic contractile ring we studied cell ghosts of the fission yeast *S. japonicus*. In normal *S. japonicus* cells many of the molecular components of the ring turn over, including the two isoforms of myosin II, Myo2 and Myp2 (28). In the fission yeast *Schizosaccharomyces pombe*, Myo2 has a turnover time of ∼19 s, while Myp2 undergoes little turnover (29, 30). Cell ghosts are prepared by enzymatic digestion of the cell walls to generate protoplasts and then permeabilizing the plasma membranes of mitotic protoplast cells to release the cytoplasm and organelles, leaving isolated membrane-bound cytokinetic rings (27, 28) (Fig. 1*B* and *Methods*). Since cytoplasm is absent there is no component association, while dissociation rates are much reduced relative to normal cells (28). Thus, cell ghosts allow the organization of isolated contractile rings to be studied in the absence of component turnover.

In Contractile Rings without Turnover, Myosin II Aggregates into Puncta with Increasing Amounts of Myosin. We imaged contractile rings in ghost cells expressing myosin II light chain Rlc1-GFP and we analyzed images from this set and from our earlier study (28). Following membrane permeabilization the myosin II distribution was mildly punctate. On incubation with

ATP, the distribution became progressively more punctate over ~30 min (Fig. 1*C* and *SI Appendix*, Fig. S6). As the punctateness increased, contractile rings suffered three distinct fates (Fig. 1*C*). Some rings appeared to remain robustly anchored to the membrane, with myosin II aggregates located around the contour defined by the initial ring. In other rings, segments appeared to detach from the membrane and straighten, presumably due to compromised anchoring to the plasma membrane that is weakened by permeabilization (31). In a third category, segments detached from the membrane and severed, following which myosin puncta in the severed segment merged with the apparently anchored segment.

For each ring we identified the longest segment attached to the membrane that neither severed nor underwent large length changes, and we measured the Rlc1-GFP intensity along the segment. Following ATP addition, peaks of myosin fluorescence intensity appeared which became increasingly prominent with time (Fig. 1*D* and *SI Appendix*, Fig. S1*A*). The relative peak amplitudes increased with time while intensity decreased in regions neighboring the peaks. The peak intensities significantly exceeded the initial intensity, indicating that the puncta were at least in part due to movement of myosin around the ring.

Thus, myosin progressively merges into aggregates of growing size in contractile rings lacking component turnover. This behavior would be expected of unopposed actomyosin contractile instability, suggesting that turnover may control the instability in normal cells.

Myosin II Aggregates Hierarchically in the Absence of Turnover. Kymographs of myosin fluorescence intensity profiles around contractile rings showed that, in regions where the myosin density was initially above the mean, the density increased in time and the region of higher density became smaller (Fig. 2*A*). In regions with an initial deficit the density decreased and the region expanded. Thus, excess density fluctuations grew and sharpened into distinct aggregates, while deficit density fluctuations diminished and became empty regions separating aggregates.

Myosin aggregated hierarchically. Neighboring aggregates moved toward one another and merged, and in some cases we observed merged aggregates themselves merging into higher-order aggregates containing yet more myosin (Fig. 2*A*). Occasionally aggregates split into two parts. The progressive, hierarchical aggregation steadily increased the mean distance between neighboring aggregates from 1.00 ± 0.28 μm to 1.77 ± 0.56 μm over 60 min (Fig. 2*B*; $n = 10$, values are mean ± SD).

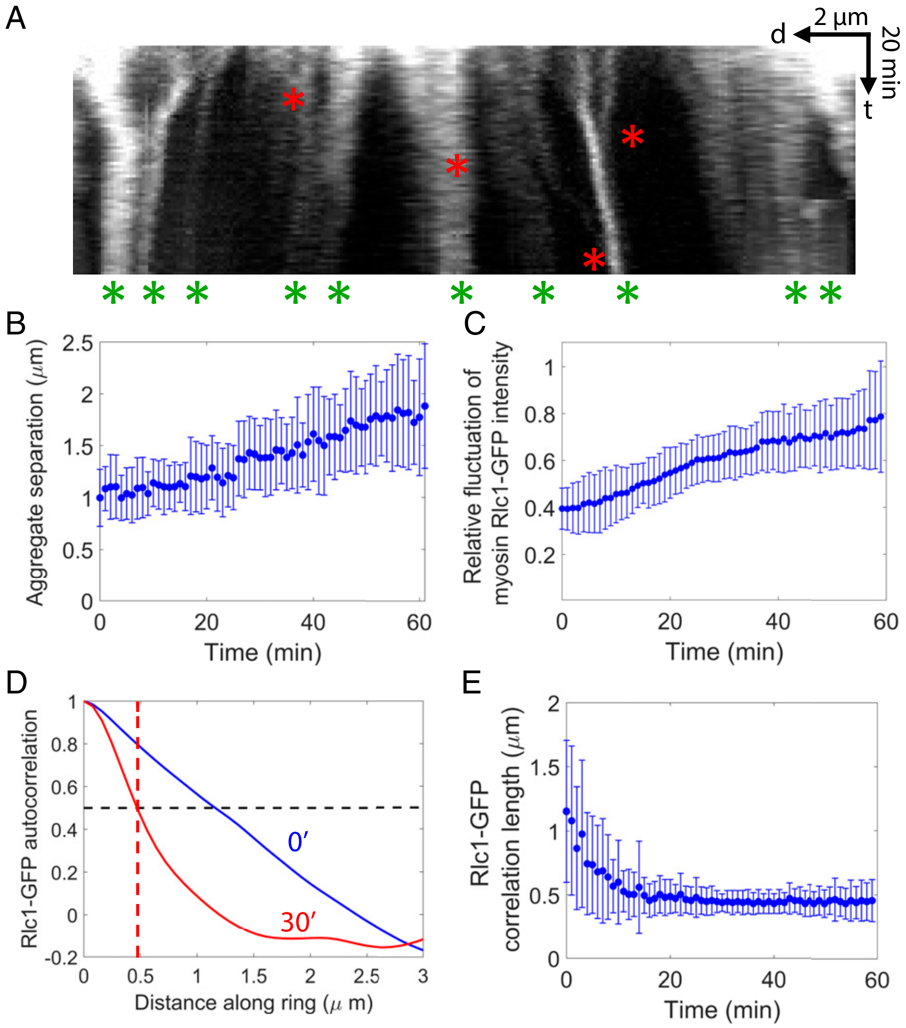

Fig. 2. Myosin II aggregates hierarchically. (*A*) Kymograph of the intact ring of Fig. 1*C*. (Time bar [t], 20 min; scale bar [d], 2 μm.) Red asterisks: hierarchical aggregation events, when two aggregates merge to form an aggregate with more myosin II. Green asterisks: aggregates at the end of the observation time (60 min). (*B*) Mean separation between myosin II aggregates versus time, averaged over all aggregates in $n = 10$ rings. (*C*) Relative fluctuation of myosin Rlc1-GFP fluorescence intensity (ratio of SD to mean) versus time in the rings of *B*. (*D*) Normalized Rlc1-GFP spatial correlations for the ring of *A* at the indicated times. The autocorrelation is the average of the product of deviations of the intensity from the mean at locations separated by a given distance around the ring, normalized to the value at zero separation. Red dashed line: the correlation length is the separation at which the correlation has decreased 50%. (*E*) Correlation length of Rlc1-GFP fluorescence intensity versus time, averaged over the rings of *B*. In *B*, *C*, and *E* error bars indicate SD.

To quantify the punctateness we measured the fluctuation in myosin fluorescence intensity relative to the mean, which increased approximately twofold over 60 min (averaged over $n = 10$ rings; Fig. 2*C*). A measure of aggregate size is the half-width of the spatial correlation function of the intensity around the ring (Fig. 2*D* and *SI Appendix*, Fig. S1*B*), which decreased from 1.15 ± 0.55 μm to 0.46 ± 0.16 μm over 60 min, with most of the decrease in the first 20 min (Fig. 2*E*; values are mean ± SD).

Molecularly Explicit Mathematical Model of the Contractile Ring in Cell Ghosts. To explore the mechanisms underlying the observed myosin aggregation (Figs. 1 and 2), we developed a three-dimensional (3D) molecularly explicit mathematical model of the cytokinetic ring in *S. japonicus* cell ghosts, closely related to our previous model of the ring of the fission yeast *S. pombe* (12, 31) (Fig. 3*A* and *SI Appendix*, Fig. S2). For details, see *Methods*. Membrane-anchored formin Cdc12 dimers anchor actin filament barbed ends to the membrane. Actin filaments dynamically cross-linked by α-actinin are bound and pulled by myosin II according to a force–velocity relation set by the measured myosin II gliding velocity (32). Myosin II is anchored to the plasma membrane in coarse-grained clusters of 8 Myo2 dimers (33), with anchor drag coefficient in the membrane chosen to be consistent with the observed aggregation times.

Throughout, we refer to these groups of eight Myo2 dimers as clusters, while the term "aggregates" will denote assemblies of several myosin clusters that merge over time (see below). For simplicity we do not attempt to model the second myosin II isoform, Myp2, which is likely unanchored from the membrane (18, 30).

To model the turnover-free situation in *S. japonicus* cell ghosts, component association is entirely absent and the ring of radius 3.7 μm does not constrict (Fig. 3*A*). Myosin, formin, and actin are present in cell ghost rings after ATP addition (28). The dissociation rate of α-actinin was taken as the value measured for *S. pombe* (12, 34), while that of myosin II was chosen to reproduce the slow decrease in total myosin II fluorescence over time measured here (*Methods* and *SI Appendix*, Fig. S3*A*). Since rings in *S. japonicus* ghosts with phallacidin-stabilized actin filaments showed negligible actin loss (28), we assumed formins do not dissociate. Rates of cofilin-mediated severing of actin filaments were set to reproduce the previously measured actin loss over ∼40 min (28). The initial ring at the instant of ATP addition was assumed normal (Fig. 1 *C* and *D*) and was generated by preequilibration of the ring for 11 min with normal component turnover, using component densities, actin filament lengths, and association rates determined by previous measurements in *S. pombe* (33, 35). In the following, images of simulated rings were convolved with a Gaussian of width 600 nm to mimic the experimental microscope point spread function (see *Methods*).

In Simulated Contractile Rings, Myosin II Aggregates Hierarchically in the Absence of Turnover. In simulations of the model, the myosin distribution evolved in very similar fashion to that seen experimentally (Figs. 1 and 2). Qualitatively similar behavior was seen in 10 simulations, as follows. Within 5 to 10 min, isolated myosin II puncta had developed (Fig. 3*B*), presumably due to the lack of component turnover. Kymographs revealed that small initial aggregates emerged from the relatively homogenous initial distribution, some of which then merged into aggregates containing more myosin (Fig. 3*C*). Some of these aggregates underwent further rounds of merging, yielding aggregates with yet more myosin. As hierarchical aggregation proceeded, peaks in the myosin density profile sharpened (Fig. 3*D* and *SI Appendix*, Fig. S4) similar to the experimental fluorescence intensity (Fig. 1*D*). As a result, relative myosin density fluctuations increased ∼2.5-fold over 60 min (Fig. 3*E*), compared with the approximately twofold experimental increase in relative myosin fluorescence intensity (Fig. 2*C*).

The distinct myosin II aggregates that emerged after 5 to 10 min had a characteristic organization, with myosin II at the center and polarity-sorted outward-pointing actin filaments (filament barbed ends colocalizing with the myosin, and distal pointed ends) (Fig. 4*A*). In a typical aggregation event, two such aggregates were pulled toward one another when the myosin in each aggregate engaged with the actin filaments hosted by the other aggregate and stepped toward the barbed ends. This occurred provided the aggregates were within a range of order the mean actin filament length of each other (Fig. 4*A*), taken as ∼1.4 μm in our simulations from measurements on *S. pombe* rings (36). Aggregates separated by more than this distance no longer affected each other, since filaments mediated the mechanical interaction. The end result of an aggregation was a similarly organized larger aggregate, with more myosin II and more polarity-sorted actin filaments.

These kinetics led to increasingly compact aggregates (Fig. 4*B*) separated by increasingly large distances (Fig. 4*C*). The size of a compact aggregate depended on the amount of myosin II it contained and the excluded volume interactions, reflecting steric interactions among myosin II molecules, which imposed a physically meaningful maximum density. The evolution of the correlation length and mean aggregate separation were both quantitatively consistent with experiment (Fig. 4 *B* and *C*).

Runaway Myosin Aggregation Leads to Ring Fracture and Tension Loss. Our experiments revealed growing myosin aggregates (Fig. 1*C*), and simulations showed progressive polarity sorting of actin filaments, with increasing colocalization of myosin and actin filament barbed ends (Fig. 4*A*). Thus, we anticipated the contractile ring tension would decrease over time, since myosin contributes less to tension when it binds and pulls a filament close to the anchored barbed end, compared with a location near the pointed end (12). We expected the tension would ultimately drop to a very low value, since the separation of the growing aggregates increased and eventually exceeded the typical actin filament length, presumably signaling ring fracture.

Measurements of simulated ring tensions confirmed these expectations. With time, the unopposed myosin aggregation destroyed the structural integrity of simulated rings and virtually abolished the ring tension. After ∼20 min rings lost mechanical connectivity (Movie S1) and ring tension decreased from ∼500 to 9 pN over 40 min (Fig. 4*D*), compared with the ∼400 pN measured in contractile rings of *S. pombe* protoplasts (12).

Runaway Aggregation Is Rescued by Myosin II Turnover but Not by Actin Turnover. Our results suggest that in normal cytokinetic rings turnover of myosin and actin protect the organization against contractile instability. We next asked if prevention of runaway aggregation required turnover of one or both of these components. In 10 cell ghost simulations with both myosin II and actin turnover restored to the values in normal intact cells, runaway aggregation was prevented and the organization was normal (Fig. 5*A*). Myosin II turnover alone [with the turnover rate measured in *S. pombe*, 0.026 s^{-1} (34)] prevented aggregation and rescued the ring organization in five other simulations (Fig. 5 *B* and *D*). However, restoring actin turnover (with turnover rates

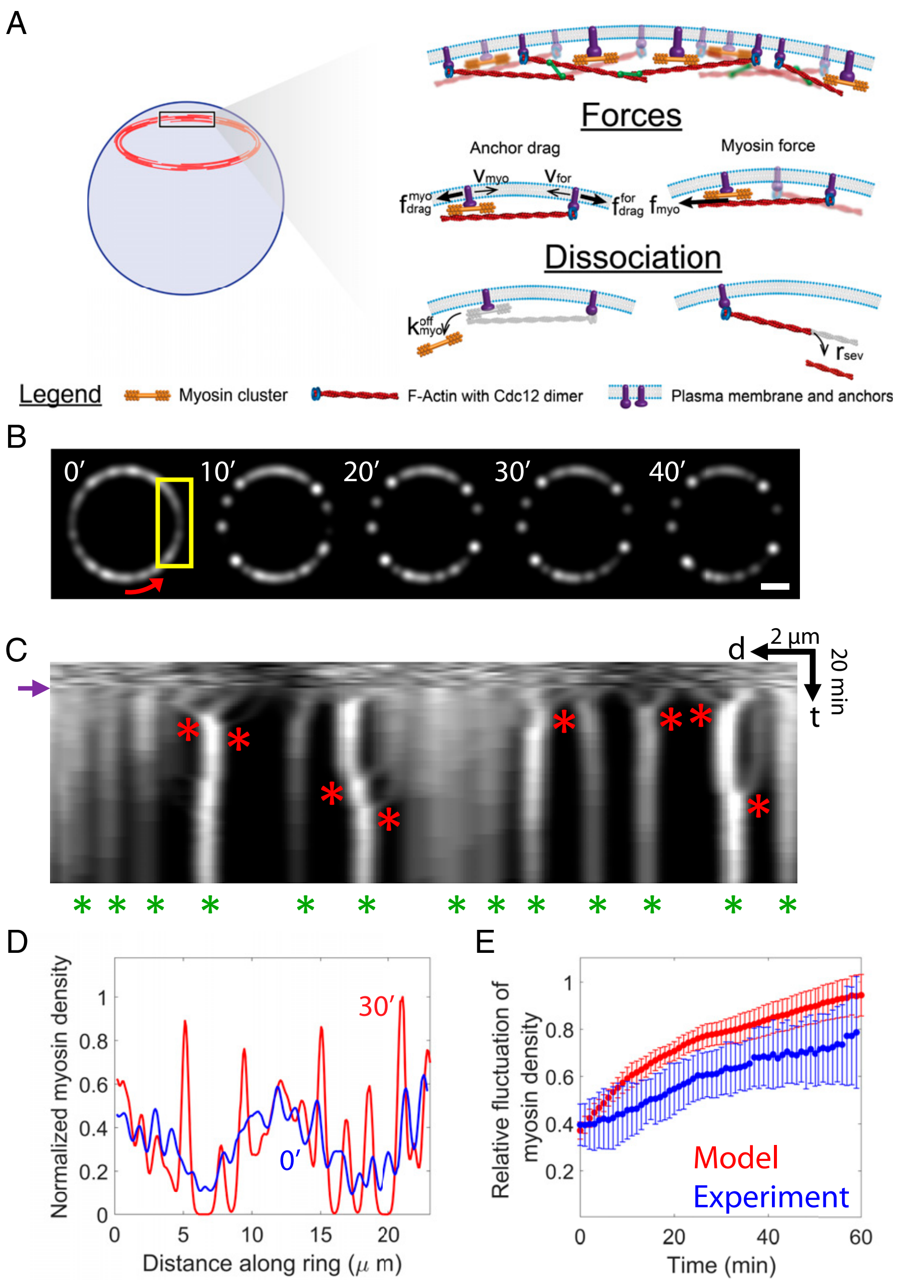

Fig. 3. Molecularly explicit mathematical model of contractile rings lacking component turnover reproduces experimental hierarchical aggregation of myosin II. (*A*) Schematic of the cell ghost contractile ring model. Components do not turn over: association is absent, and dissociation is much slower than normal (see main text). Barbed-end anchored actin filaments bind and are pulled by membrane-anchored myosin II. Component motions are resisted by drag from the plasma membrane on membrane anchors. (*B*) Myosin II distributions from simulations of the model. Simulated confocal fluorescence images are shown, using a point spread function of full width half maximum 600 nm similar to that of the microscope used for experimental images. The ring was run to steady state for 11 min under normal turnover conditions. Turnover was then abolished at $t = 0$. Red arrow: coordinate along ring. (Scale bar, 2 μm.) (*C*) Kymograph of the ring of *B*. (Time bar [t], 20 min; scale bar [d], 2 μm.) After turnover is switched off (purple arrow), myosin II aggregates (red asterisks). Hierarchical aggregation leaves a diminished number of aggregates at the end of the simulation period (green asterisks). (*D*) Relative myosin II density versus distance around the ring of *B* at the indicated times. Densities are normalized so that the maximum density at 30 min is unity. (*E*) Simulated relative myosin II density fluctuations (ratio of SD to mean) versus time, averaged over $n = 10$ simulated rings. Experimental data of Fig. 2*C* shown for comparison. Error bars indicate SD.

consistent with experimental measurements in *S. pombe*; see *Methods*) failed to rescue rings from catastrophic aggregation in another five simulations (Fig. 5*C*). In the latter case, compared with cell ghosts late-stage aggregates had a larger separation (Fig. 5*E*), since actin turnover maintained longer filaments that allowed myosin aggregates to communicate over greater distances, and the rate of tension loss was lower (*SI Appendix*, Fig. S3*C*). Thus, myosin II turnover but not actin turnover is sufficient to prevent runaway aggregation. In ring simulations using a range of turnover times interpolating between the extremely small values in cell ghosts and the values in normal cells (*SI Appendix*, Table S1), myosin aggregation effects were apparent for myosin turnover times approximately fivefold the normal value or greater, while ring morphology was insensitive to the actin turnover time (*SI Appendix*, Fig. S5 and *Methods*).

Hierarchical Aggregation Is Progressively Slowed Down by Increasing Degrees of Myosin II Inhibition. These simulation results suggest that myosin II contractile forces drive the aggregation observed in the absence of turnover. Thus, we would

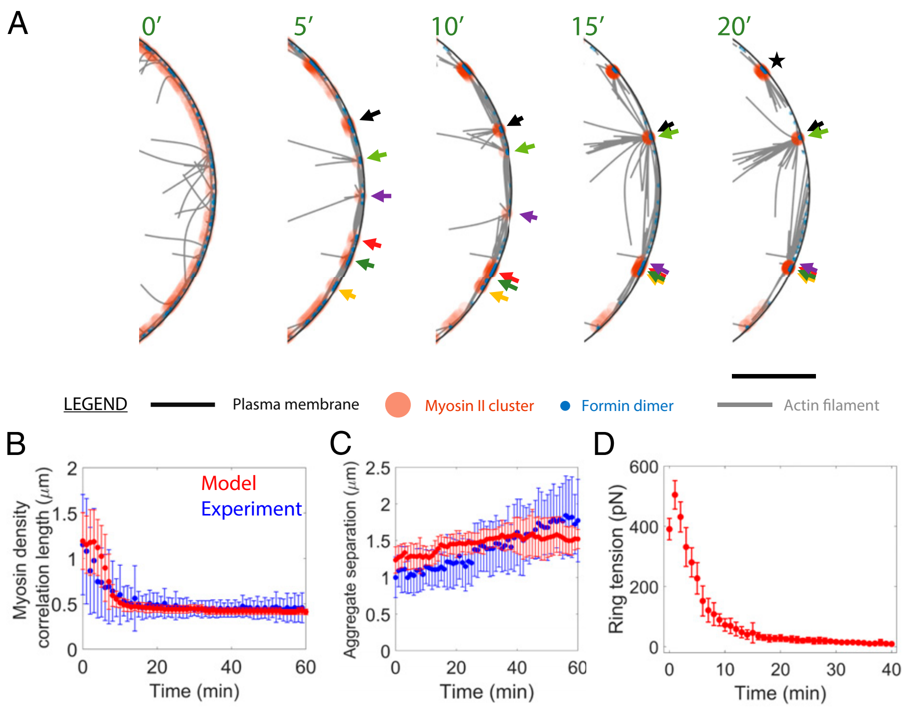

Fig. 4. Actin filaments mediate mechanical communication among aggregates and set the aggregation range. (*A*) Section of the simulated cell ghost contractile ring of Fig. 3*B* (yellow box) at the indicated times. Myosin II aggregates progressively merge into more substantial aggregates (arrows; each color tracks a specific initial aggregate). The process continues until the large aggregates are no longer connected by actin filaments (e.g., aggregate labeled ★), when the ring fractures with tension loss. Formin dimer size and actin thickness not to scale. Model parameters as in *SI Appendix*, Table S1. (Scale bar, 1 μm.) (*B*) Myosin II density correlation length versus time averaged over the 10 simulated rings of Fig. 3*E*. Experimental data of Fig. 2*E* shown for comparison. (*C*) Mean myosin II aggregate separation versus time averaged over the simulated and experimental rings of Figs. 2*B* and 3*E*, respectively. (*D*) Mean ring tension versus time averaged over the simulated rings of Fig. 3*E*. ATP is added at time 0. Over 40 min the tension decreases to ∼9 pN. Switching off actin filament elongation causes a very early transient tension increase. In *B*–*D* error bars are SD.

expect aggregation to be progressively curtailed by increasing doses of the myosin II inhibitor blebbistatin. We simulated blebbistatin effects by turning off forces exerted on actin filaments by a randomly selected subset of myosin clusters whose identity was refreshed every second, since experiments show blebbistatin biases myosin to a state interacting weakly with actin filaments (37, 38). The fraction of deactivated myosin was varied, to mimic increasing blebbistatin levels. To quantify the degree of aggregation we counted the number of myosin gaps in contractile rings, defined as regions of width 600 nm or greater lacking myosin. After 9 min of simulation, all rings developed at least one gap for myosin deactivation levels 10% or lower (*SI Appendix*, Fig. S6*B*). For deactivation levels 30%, 50%, 70%, and 90%, gaps had appeared after 9 min in four, three, one, and zero rings, respectively, out of five rings for each deactivation level. Thus, simulations show slower aggregation when myosin is partially deactivated.

To compare these model results with experiment we imaged rings in cell ghosts treated with blebbistatin at concentrations 0 to 40 μM prior to ATP-mediated activation (see *Methods*). After 9 min, two of three rings with no blebbistatin had already developed gaps; one out of four rings had developed a gap for 10 μM blebbistatin, and no gaps had developed for 25 μM and 40 μM blebbistatin (in seven and four rings, respectively) (*SI Appendix*, Fig. S6*A*). Thus, consistent with simulations, increasing levels of blebbistatin-mediated myosin deactivation progressively slowed down aggregation of myosin.

Myosin Diffusion Is Too Weak to Prevent Runaway Aggregation Due to Contractile Instability. The present work implicates myosin II turnover as the mechanism that controls contractile instability in cells. It has been suggested that myosin II diffusivity serves this purpose, by smoothing small-scale density variations that characterize the instability (15, 26). To test this proposal we ran simulations of contractile rings without turnover as previously, but now the membrane-anchored myosin II clusters could diffuse laterally in the membrane with diffusivity D.

We tested diffusivities in the range $10^{-5} \leq D \leq 10^{-2}\ \mu\mathrm{m}^2 \cdot \mathrm{s}^{-1}$ (Fig. 6). In five simulations per diffusivity value, myosin aggregation was not prevented by diffusion, except for the highest values tested $D \sim 10^{-2} \mu\mathrm{m}^2 \cdot \mathrm{s}^{-1}$. This value is almost three orders of magnitude greater than measured diffusivities of membrane-bound myosin II in fission yeast contractile rings, $D \sim 2 \times 10^{-5} \mu\mathrm{m}^2 \cdot \mathrm{s}^{-1}$ (39). We conclude that physiologically relevant myosin diffusion is far too weak to oppose contractility-induced aggregation.

Discussion

The cytokinetic contractile ring and other actomyosin machineries require mechanisms to intercept contractile instability (Fig. 1*A*), but these have been difficult to identify since the full course of the instability is rarely observed. Here, we observed the instability run its full course in isolated contractile rings in cell ghosts, from initially normal organization to a final catastrophically disrupted dead-end state. In a hierarchical process, myosin II aggregated into puncta that merged with one another, some of these larger aggregates merging into yet larger aggregates, and so on (Fig. 2*A*). Aggregation progressively increased the myosin per aggregate and the aggregate separation, up to ∼1 to 2 μm (Fig. 2*B*). We observed no greater separations, suggesting that this separation effectively terminated the process, consistent with simulations which identified the maximum separation as the mean actin filament length (Fig. 5).

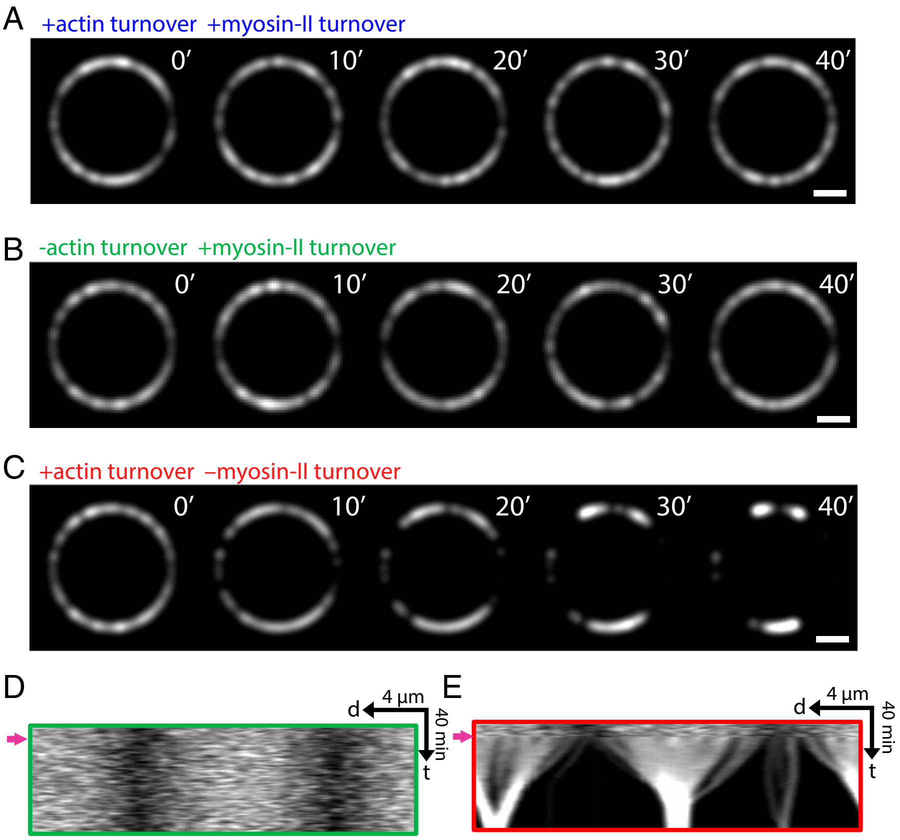

Fig. 5. Runaway aggregation is rescued by myosin II turnover but not by actin turnover. (*A*–*C*) Simulated confocal fluorescence micrographs of myosin II in cell ghosts with either myosin II turnover restored (*B*), or actin turnover restored (*C*), or turnover of both components restored (*A*). (Scale bar, 2 µm.) (*D* and *E*) Kymographs of the rings of *B* and *C*, respectively. Arrows indicate the instants when the respective turnover conditions were implemented.

Here, hierarchical aggregation is driven by active myosin-mediated contractile forces. It is of interest to compare this with analogous systems where the driving forces are passive particle–particle adhesive interactions, well known in contexts such as aggregation of atmospheric pollutant particles or colloidal suspensions (40). In these cases larger aggregates are effectively more adhesive due to their greater surface area, which can lead to hierarchical kinetics dominated by ever-larger aggregates (41).

We reasoned that the uncontrolled aggregation was caused by the absence of component turnover. Since cell ghosts lack cytoplasm, association of myosin II, actin and other components is absent and component dissociation rates are severely reduced. Turnover would tend to restore homogeneity to the ring, so its absence could explain the runaway aggregation. Molecularly explicit simulations corroborated this interpretation (Figs. 3–6). Simulations of cell ghost rings lacking turnover quantitatively reproduced the experimental hierarchical myosin aggregation. Aggregates emerged from local stochastic myosin density peaks that drew in myosin and actin filaments (Fig. 1*A*). Late-stage aggregates had a myosin II core and outward pointing polarity-sorted actin filaments. Interestingly, some late aggregates had an aster structure, with a relatively compact myosin core and actin filaments pointing radially outward in multiple directions (Fig. 4*A*), similar to in vitro actomyosin systems which evolved to a final state consisting of morphologically quiescent asters with polarity sorted actin filaments (42). Other late aggregates had a more extended myosin II core, with longitudinally oriented actin filaments emerging at the edges (Fig. 4*A*).

Hierarchical aggregation, in which aggregates repeatedly merged into yet larger aggregates, continued until the aggregate separation exceeded the typical actin filament connector length when aggregates could no longer communicate mechanically. As aggregates became mechanically isolated, the ring tension decayed to zero and the ring fractured (Fig. 4). In this dead-end state the contractile instability had run its full course, with morphologically quiescent aggregates similar to those observed in vitro (42).

By contrast, in simulations of rings in normal cells with turnover, myosin reached a steady-state punctateness with moderately sized aggregates (Fig. 5*A*). Myosin II turnover was the key process averting runaway aggregation, by replacing large myosin aggregates with more homogenously distributed moderately sized aggregates, before hierarchical aggregation could run its catastrophic course. When actin turnover was switched off, turnover of myosin II alone was sufficient to prevent aggregation (Fig. 5 *B* and *D*). Actin turnover alone was insufficient to prevent aggregation (Fig. 5 *C* and *E*). Simulations assumed myosin and actin turn over independently, consistent with experiments showing myosin Myo2 is anchored to the plasma membrane in the fission yeast ring (33) and remains in the ring following actin disassembly by latrunculin A treatment (18).

We conclude that rapid myosin turnover in contractile rings prevents runaway aggregation and tension loss. While not the emphasis of this study, normal cytokinesis also requires actin turnover (28), and contractile ring homeostasis in normal cells likely relies on turnover of both myosin II and actin in complimentary ways. In fission yeast, contractile rings are assembled from a ∼2-µm-broad band of precursor protein complexes called nodes containing myosin and other components. Nodes grow actin filaments to assemble the nodes into a narrow ring, and experimental and computational observations suggest sufficiently rapid actin turnover is required to avoid unproductive

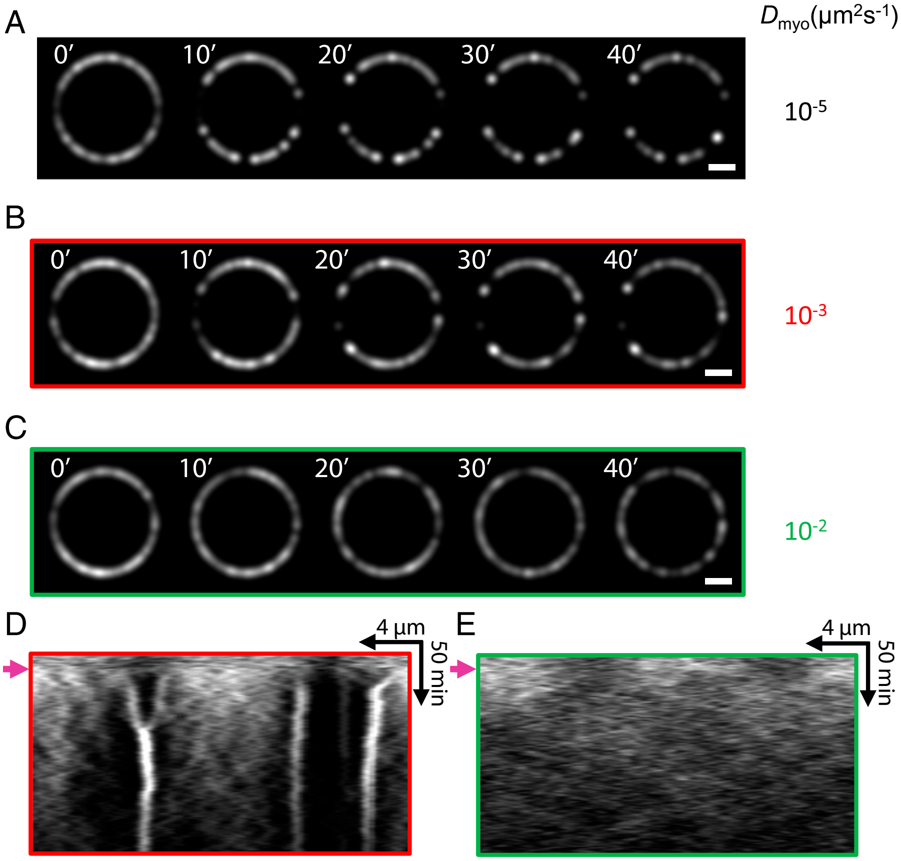

Fig. 6. Myosin II diffusion does not prevent runaway aggregation due to contractile instability. (*A*–*C*) Simulated confocal fluorescence micrographs of myosin II in cell ghost contractile rings that lack turnover, with lateral diffusion of myosin II aggregates in the plasma membrane implemented. Three diffusivities were simulated, $D_{\text{myo}} = 10^{-5}$, 10^{-3}, and $10^{-2} \mu m^2 \cdot s^{-1}$. Myosin diffusion rescues the normal myosin II distribution only for the largest diffusivity, a value ~500-fold larger than physiological values measured in fission yeast *S. pombe* (39). (Scale bar, 2 μm.) (*D* and *E*) Kymographs of the rings of *B* and *C*, respectively. Arrows indicate instants at which turnover is switched off.

node aggregation (39, 43). In mutants of the actin-severing protein cofilin that contributes to actin turnover, contractile rings suffer structural instabilities in which actin bundles peel away from the plasma membrane into straight bridges (43–45) containing Myp2 but not Myo2 (44). We recently modeled these mutants and concluded that bridging instability originates in ring tension being higher due to the longer actin filaments, generating higher centripetal forces that pull Myo2-anchored actin filaments away from the membrane (46). Our previous experimental work emphasized the role of actin turnover for normal organization and function of contractile rings (28). Myosin II aggregation in *S. japonicus* cell ghosts was abolished by treatment with the myosin II inhibitor blebbistatin, and stabilization of actin with jasplakinolide suppressed formation of small myosin puncta and increased the fraction of rings that shortened. These rings appeared to fully constrict, but broad myosin II aggregates were apparent in these shortening rings, similar to our simulations with restored actin turnover (compare Figs. 3*B* and 5*C*). The shortening segments in these rings likely have zero tension, since a mathematical model (31) of the analogous phenomenon seen experimentally (27) in *S. pombe* fission yeast ghosts accurately reproduced the observed shortening rates and showed that rings shortened due to zero tension detached segments being reeled in by myosin II against zero load.

We have found that myosin turnover protects contractile rings from large-scale contractile instabilities that would provoke aggregation. Contractile instability also affects the smallest scales since, if unopposed, it would aggregate myosin II into clumps of arbitrarily high density (see Fig. 1*A*). In simulations without turnover, aggregate sizes were set by the amount of myosin II in the aggregates, excluded volume interactions and local polarity sorting (Fig. 4*A*). Our results suggest that in the cytokinetic ring and other actomyosin machineries, small-scale contractile instability is controlled by several small-scale effects. These include excluded volume interactions due to steric intermolecular interactions that impose packing limits, small-scale actomyosin polarity sorting that suppresses contractility (42), and other local interactions such as myosin II minifilament stacking in animal cells (47).

It is often assumed that myosin diffusion provides this small-scale control. Active gel models of actomyosin cortices commonly assume a diffusive contribution to the myosin motion, which helps suppress actomyosin instability that would otherwise cause uncontrolled short scale density blow up (15, 26). To be effective, diffusivities of order $D \sim 0.01\ \mu m^2 \cdot s^{-1}$ or larger are invoked. However, measured myosin II diffusivities in contractile rings in fission yeast (39) are $\sim 2 \times 10^{-5}\ \mu m^2 \cdot s^{-1}$, ~3 orders of magnitude smaller, and were reported unmeasurably small in the *C. elegans* embryo cortex (16). Thus, myosin diffusivity is presumably not responsible for controlling actomyosin contractile instability, and its inclusion in models is a numerical convenience that misrepresents at least the small-scale behavior. We confirmed this in simulations with added myosin cluster diffusivity. A diffusivity ~500 times larger than the experimental value was required to prevent uncontrolled aggregation (Fig. 6).

Overall, our results suggest that in actomyosin assemblies a balance of turnover and small-scale effects regulates contractile instability on large and small scales, respectively (Fig. 7). We

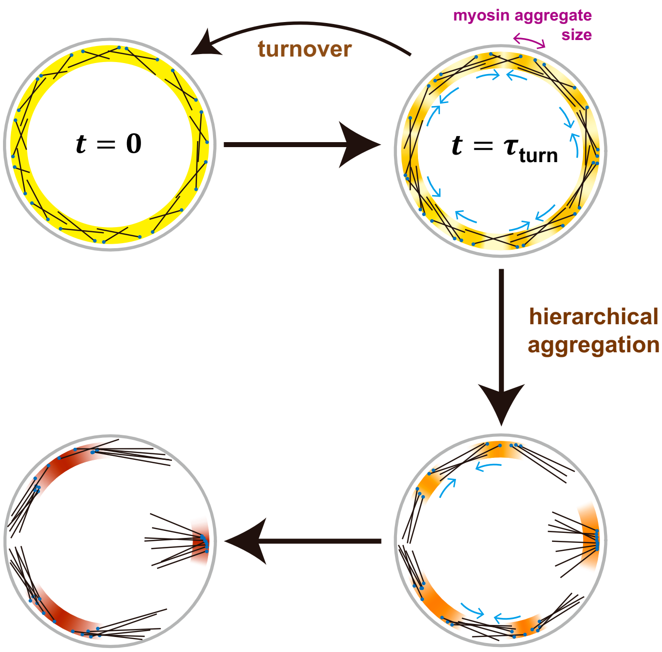

Fig. 7. Turnover regulates contractile instability to set myosin II aggregate size and prevent runaway aggregation. Model of turnover-regulated contractile instability. Contractile instability progressively increases punctateness in the contractile ring and other actomyosin machineries. Given a homogenous initial distribution ($t = 0$), in normal cells component turnover tends to restore homogeneity by intercepting the instability on the turnover timescale τ_{turn}, setting a functional steady state myosin II aggregate size. Without turnover contractile instability progresses unopposed, separating the aggregates and hierarchically merging them into yet bigger aggregates with increased separation. Late-stage aggregates have a myosin II core and outward pointing polarity-sorted actin filaments, with a size governed by local excluded volume interactions that cap the density and polarity sorting that effectively switches off contractility. Once the aggregate separation exceeds the actin filament length aggregates can no longer communicate mechanically, and contractile instability has run its full course (*Bottom Left*). Schematic depicts myosin density (yellow/orange/brown shading), actin filaments (black), and membrane-anchored actin filament barbed ends (blue).

suggest contractile instability serves the useful function of assembling myosin II into force-generating aggregates, regulated by turnover which imposes a time limit on the contractile instability-driven aggregation. The steady-state myosin aggregate size is set by the turnover time, together with local effects that dictate a maximum density of actomyosin components. The turnover time allows aggregation to proceed for long enough that powerful myosin aggregates are built, but short enough to prevent runaway aggregation and disastrous organizational disruption, tension loss and ring fracture (Fig. 7).

Methods

1. *S. japonicus* Cell Ghost Preparation and ATP-Dependent Ring Activation. *S. japonicus* cell ghosts were prepared using protocols published previously (48, 49). A brief summary is given below. For strains, see ref. 28. *S. japonicus* cells were cultured until midlog phase using a rich YEA medium, and cell walls were digested using lytic enzymes Lallzyme MMX (Lallemand; ref. 50) for protoplast preparation. Protoplasts were then washed and recovered in sorbitol-containing medium. Following ring assembly, protoplasts were washed once with wash buffer (20 mM Pipes-NaOH, pH 7.0, 0.8 M sorbitol, 2 mM EGTA, and 5 mM $MgCl_2$) and permeabilized with isolation buffer (50 mM Pipes-NaOH, pH 7.0, 0.16 M sucrose, 50 mM EGTA, 5 mM $MgCl_2$, and 50 mM potassium acetate) containing 0.5% Nonidet P-40 to obtain cell ghosts. Ghosts were washed twice with reactivation buffer (0.16 M sucrose, 5 mM $MgCl_2$, 50 mM potassium acetate, and 20 mM MOPS-NaOH, pH 7.0; pH adjusted to 7.5) after permeabilization. Both the isolation and reactivation buffers were cooled to 4 °C. The isolation and washing steps were performed on ice. Equal volumes of cell ghosts and reactivation buffer containing 1 mM ATP (A6559; Sigma-Aldrich) were then mixed to induce ATP-dependent actomyosin contractile forces in the ring. It takes at least 1 to 2 min after the addition of ATP to mount the ghosts and to find those appropriate for imaging. Thus, time 0 in figures represents the instant at which imaging commences.

Cytokinetic ring constriction in the presence of blebbistatin. The cytokinetic rings were isolated from *S. japonicus* ghost cells using the protocol mentioned in Huang et al. (48, 49). The isolated rings were mixed with different concentrations (0, 10, 25, and 40 mM) of blebbistatin (B0560; Sigma). The rings were then activated with 0.5 mM ATP (A6559; Sigma) and imaged using the Andor Revolution XD spinning disk confocal system, equipped with an Andor iXon Ultra EMCCD (electron-multiplying charge-coupled device) camera. The images were captured with a Z-step size of 0.5 µm for 25 min. The images were projected along the *z* axis by Fiji.

2. Sample Preparation for Microscopy Imaging. An equal volume of reactivation buffer containing 1 mM ATP was added to cell ghosts and imaging was performed in an Ibidi µ-Slide eight-well glass-bottom dish (80827). To prevent water evaporation during imaging, an adhesive film membrane was used to seal all imaging dishes.

3. Spinning-Disk Confocal Microscopy. Image acquisition was performed using Andor Revolution XD spinning-disk confocal microscopy. The microscope was equipped with a Nikon Eclipse Ti inverted microscope, Nikon Plan Apo Lambda 100×/1.45 numerical aperture oil-immersion objective lens, a spinning-disk system (CSU-X1; Yokogawa Electric Corporation), and an Andor iXon Ultra EMCCD camera. Andor IQ3 software was used to acquire images at 80 nm/pixel. Laser lines at wavelength of 488 nm were used to excite the fluorophores. Most images were acquired with *z*-step sizes of 0.5 µm, and at an interval time of 1 min.

4. Three-Dimensional Molecularly Explicit Model of the Cytokinetic Ring in *S. japonicus*. We developed a fully 3D and molecularly explicit mathematical model of the *S. japonicus* cytokinetic ring. Formin Cdc12 dimers anchored to the membrane nucleate and grow actin filaments that bind myosin II, assumed membrane-anchored from previous studies. In this section, we describe the model for a normal ring with normal turnover processes, as realized in normal intact cells or protoplasts. Later sections describe the model's adaptation to the situation in cell ghosts where turnover processes are switched off.

4.1. Ring geometry. The ring lies on the inner surface of the plasma membrane. Ring components bind with uniform probability in a binding zone of width 0.2 µm (12, 35) on the plasma membrane, thus determining the width of the ring. The thickness of the ring in the direction perpendicular to the plasma membrane is an output of the simulation dynamics. We used a ring radius of 3.7 µm as the rings we observe here have a mean length up to ∼22 to 25 µm.

4.2. Components in the ring. We describe actin filaments as inextensible but flexible polymers with bending modulus $\kappa = k_B T l_p$ where the persistence length $l_p = 10$ µm (51, 52). In the simulation, we keep track of every 37th actin subunit on a filament, with spacing 0.1 µm from each other, as in our earlier work (12, 31). The subunits at the barbed end of each filament represent formins, which are anchored to the plasma membrane and subject to anchoring drag.

Myosin II in the ring is described as clusters containing 16 myosin heavy chains (31) and are anchored to the plasma membrane and subject to anchoring drag (12). A cluster binds and pulls on actin filaments within its capture radius $r_{myo} = 80$ nm measured from the center of the cluster (53).

Alpha-actinin cross-linkers are modeled as springs with rest length $r_x^0 = 30$ nm and spring constant $k_x = 25$ pN/µm, connecting pairs of actin subunits (only those that we keep track of) on different filaments that are within distance $r_x^{bind} = 50$ nm from each other.

4.3. Forces in the ring.

Binding of actin filaments to myosin clusters. A myosin II cluster α binds and exerts a capture force $\mathbf{f}_{i,\alpha}^{cap}$ on every actin subunit i within its capture radius r_{myo}, implemented as a spring with spring constant $k_{cap} = 400$ pN/µm and zero rest length that connects the center of the cluster $\mathbf{r}_\alpha$ to the actin subunit located at $\mathbf{r}_i$. In order not to interfere with the pulling force of the myosin, we decompose this force along and perpendicular to the actin filament, and only the latter is actually applied:

$$\boldsymbol{f}_{i,\alpha}^{\mathbf{cap}} = -k_{\mathrm{cap}} \left\{ (\boldsymbol{r}_i - \boldsymbol{r}_\alpha) - [(\boldsymbol{r}_i - \boldsymbol{r}_\alpha) \cdot \hat{\mathbf{T}}_i]\hat{\mathbf{T}}_i \right\},$$

where $\hat{\mathbf{T}}_i$ is the unit tangent vector of the actin filament at subunit i.

Force–velocity relation of myosin. Myosin II cluster α pulls on bound actin subunits i with a force tangent to the filament:

$$\boldsymbol{f}_{i,\alpha}^{\mathbf{pull}} = f_{\mathrm{s}} \left[1 - \frac{(\boldsymbol{v}_i - \boldsymbol{v}_\alpha) \cdot \hat{\mathbf{t}}_i}{v_{\mathrm{myo}}^0} \right] \hat{\mathbf{t}}_i,$$

where $\hat{\mathbf{t}}_i$ is the unit vector from the $(i-1)^{\mathrm{th}}$ subunit to the i^{th} subunit. This force decreases linearly with the velocity that the myosin II cluster moves toward the barbed end $(\boldsymbol{v}_i - \boldsymbol{v}_\alpha)$ and is equal to the stall force $f_{\mathrm{s}} = 4$ pN or zero when the velocity is equal to zero or the load-free velocity v_{myo}^0, respectively. When one myosin II cluster pulls on $n_{\mathrm{fil}} > 10$ actin filaments, the stall force is lowered to a value $f_{\mathrm{s}} = (4 \text{ pN}) \times (10/n_{\mathrm{fil}})$.

Excluded volume interactions. Myosin II clusters repel other clusters located within a distance $d_{\mathrm{myo}} = 45$ nm, with an elastic force that increases linearly as the distance decreases. The elastic constant $k_{\mathrm{myo}}^{\mathrm{excl}} = 4$ pN/nm. The value of the distance was chosen so that the aggregates from the simulation and experiment had a similar morphology, which is a mix of broad and point-like aggregates.

Tension in actin filaments and ring tension. Tension is implemented as pairwise attractive force of magnitude $f_{i,i+1}^{\mathrm{tension}}$ between adjacent actin subunits labeled by i and $i+1$. The constraint force ensures that the subunit separation is maintained at 0.1 μm (see subsection 4.2). The force is implicitly set by the dynamics, and in practice is calculated together with component velocities. See *Numerical scheme*. The sum of filament tension forces exerted across each ring cross-section were obtained and averaged over all cross-sections to obtain ring tension at every time instant.

Bending forces of actin filaments. Following the scheme in ref. 54, first the bending energy of one filament is calculated as

$$H^{\mathrm{B}} = \frac{\kappa}{l_0} \sum_{i=2}^{N-1} \left(1 - \hat{\mathbf{t}}_i \cdot \hat{\mathbf{t}}_{i-1}\right).$$

The filament has N subunits, each separated by $l_0 = 0.1$ μm, and a bending modulus κ. The bending force is given by $-(\partial H^{\mathrm{B}})/(\partial \boldsymbol{r}_i)$, the negative derivative of H^B with respect to the coordinates of the subunits.

Cross-linking. Cross-linkers exert a spring force $\boldsymbol{f}_i^{\mathbf{x}}$ between actin subunits. See subsection 4.2 for details.

Ring component confinement. This constraint is implemented as an elastic restoring force with elastic constant $k_{\mathrm{mb}} = 20$ pN/μm pointing toward the origin that is activated when any ring component is greater than R away from the origin, where R is the radius of the cell.

Normal anchoring forces. Formin Cdc12 dimers and myosin II clusters are anchored to the plasma membrane (33), and an anchoring force normal to the plasma membrane maintains their radial coordinate at $R - d_{\mathrm{for}}$ and $R - d_{\mathrm{myo}}$ respectively, where $R, d_{\mathrm{for}}, d_{\mathrm{myo}}$ are the radius of the cell, and distances of formin and myosin from the membrane, respectively. The magnitude of this force is implicitly set by the dynamics, and in practice is calculated together with component velocities. See *Numerical scheme*. The values of d_{for} and d_{myo} are 30 nm and 80 nm, respectively, based on superresolution measurements (33).

Tangential anchoring forces due to membrane drag. As all formin Cdc12 dimers and myosin II clusters are membrane anchored, they experience drag forces $\boldsymbol{f}_{\mathbf{for}}^{\mathbf{drag,\ mb}} = -\gamma_{\mathrm{for}}\boldsymbol{v}$ and $\boldsymbol{f}_{\mathbf{myo}}^{\mathbf{drag,mb}} = -\gamma_{\mathrm{myo}}\boldsymbol{v}$, respectively.

Cytosolic drag forces. Drag forces for actin subunits in the cytosol are set by their velocities and the drag coefficient $\gamma_{\mathrm{act,proto}} = 0.2 \text{ pN} \cdot \text{s} \cdot \mu\text{m}^{-1}$ (12). Cytosolic drag forces for myosin II clusters and formin Cdc12p dimers are neglected as they are much smaller than the membrane drag force.

Stochastic forces. A myosin II cluster α of the simulations in Fig. 6 has a diffusivity D due to a newly added stochastic, zero-mean force $\boldsymbol{f}_{\boldsymbol{\alpha}}^{\mathbf{diff}}$. The correlation of the force is given by $\langle \boldsymbol{f}_{\boldsymbol{\alpha}}^{\mathbf{diff}}(t)\boldsymbol{f}_{\boldsymbol{\alpha}'}^{\mathbf{diff}}(t') \rangle = D_{\mathrm{myo}}\gamma_{\mathrm{myo}}^2 \delta(t-t')\delta_{\alpha\alpha'}\boldsymbol{I}$ where γ_{myo} and $\boldsymbol{I}$ are, respectively, the drag coefficient parallel to the membrane and the 3×3 matrix whose only nonzero entries are $I_{\mathrm{xx}} = I_{\mathrm{yy}} = 1$.

4.4. Turnover of ring components. Formin Cdc12p dimers, myosin II clusters, and α-actinin cross-links dissociate from the ring at rates $k_{\mathrm{off,proto}}^{\mathrm{for}}$, $k_{\mathrm{off,proto}}^{\mathrm{myo}}$, and $k_{\mathrm{off}}^{\mathrm{x}}$, respectively. In addition, α-actinin unbinds the ring if the two actin subunits that it cross-links are separated by $> r_{\mathrm{x}}^{\mathrm{bind}} = 50$ nm. Formin Cdc12 dimers and myosin II clusters bind the plasma membrane in a binding zone of width 0.2 μm. Alpha-actinin cross-links bind the ring with equal probability between any pair of actin subunits within $r_{\mathrm{x}}^{\mathrm{bind}}$ unless this pair has already been cross-linked. Component binding rates are chosen to maintain steady state of component densities (*SI Appendix*, Table S1). Cross-linker binding rates are tuned to achieve a steady-state cross-linker density of $25 \ \mu\text{m}^{-1}$ (35).

Actin is polymerized by formin at $v_{\mathrm{pol}} = 70$ nm/s and subject to severing by ADF-cofilin at rate $r_{\mathrm{sev,proto}} = 1.8 \ \mu\text{m}^{-1} \cdot \text{min}^{-1}$, at a random location along the filament with uniform probability (12). Once severed, the portion from the severing point to the pointed end is removed from the simulation.

Mean actin filament length in simulations is ∼1.4 μm, and is set by formin density, filament growth rate, and filament severing rate. (1) Previously measured formin densities are ∼15 per micrometer (*SI Appendix*, Table S1). (2) Electron micrographs showed ∼20 filaments in the cross section of the *S. pombe* ring (55). (3) Upon addition of the actin monomer sequestering drug latrunculin A to intact cells, in 60 s, ∼90% of cells lost their rings (56). The growth and severing rates v_{pol} and r_{sev} were obtained as best-fit parameters to reproduce (2) and (3) above.

The initial experimentally measured Rlc1-GFP fluorescence distribution had a correlation length ∼1.0 μm (Fig. 2*E*). In our simulations we used a simple measure to reproduce these statistics. We divided the perimeter of the simulated ring into four equal sectors and chose the association kinetics such that incoming myosin clusters had a preference to bind to two nonneighboring sectors. This generated steady-state rings with a correlation length of myosin density at $t = 0$ similar to that seen experimentally before turnover was abolished (Fig. 4*B*). Irrespective of whether or not we used such a spatial turnover bias to set up the initial state of the ring, we observed the same hierarchically aggregating myosin behavior once turnover was switched off.

4.5. Simulation of the model.

Initial configuration of the ring. The ring is initially a 0.2-μm-wide bundle composed of myosin II clusters and actin filaments that have a clockwise or anticlockwise orientation with equal probability. Their barbed ends (formin Cdc12p dimers) and myosin II clusters are randomly distributed in a band-like zone 0.2 μm wide on the plasma membrane, with uniform probability per area. Eleven minutes of ring dynamics is simulated in order for the ring to reach steady state.

Numerical scheme. Given the ring configuration at any time step, we numerically solve the linear system of force balance equations

$$\begin{cases} \displaystyle\sum_\alpha \left[\boldsymbol{f}_{i,\alpha}^{\mathbf{cap}} + \boldsymbol{f}_{i,\alpha}^{\mathbf{pull}}(\boldsymbol{v}_i, \boldsymbol{v}_\alpha)\right] - \frac{\partial H^{\mathrm{B}}}{\partial \boldsymbol{r}_i} + f_{i,i+1}^{\mathrm{tension}} \frac{\boldsymbol{r}_{i+1} - \boldsymbol{r}_i}{|\boldsymbol{r}_{i+1} - \boldsymbol{r}_i|} + \boldsymbol{f}_i^{\mathbf{mb}} + f_i^{\mathrm{anch}}(\boldsymbol{r}_i)\hat{\boldsymbol{r}} + \boldsymbol{f}_{\mathbf{for}}^{\mathbf{drag,mb}}(\boldsymbol{v}_i) = 0, \\ \qquad\qquad \text{for anchored formin } i \\ \displaystyle\sum_\alpha \left[\boldsymbol{f}_{i,\alpha}^{\mathbf{cap}} + \boldsymbol{f}_{i,\alpha}^{\mathbf{pull}}(\boldsymbol{v}_i, \boldsymbol{v}_\alpha)\right] - \frac{\partial H^{\mathrm{B}}}{\partial \boldsymbol{r}_i} + f_{i,i+1}^{\mathrm{tension}} \frac{\boldsymbol{r}_{i+1} - \boldsymbol{r}_i}{|\boldsymbol{r}_{i+1} - \boldsymbol{r}_i|} + f_{i-1,i}^{\mathrm{tension}} \frac{\boldsymbol{r}_{i-1} - \boldsymbol{r}_i}{|\boldsymbol{r}_{i-1} - \boldsymbol{r}_i|} + \boldsymbol{f}_i^{\mathbf{x}} + \boldsymbol{f}_i^{\mathbf{mb}} + \boldsymbol{f}_i^{\mathbf{visc}}(\boldsymbol{v}_i) = 0, \\ \qquad\qquad \text{for actin subunit } i \text{ not at the pointed end} \\ \displaystyle\sum_\alpha \left[\boldsymbol{f}_{i,\alpha}^{\mathbf{cap}} + \boldsymbol{f}_{i,\alpha}^{\mathbf{pull}}(\boldsymbol{v}_i, \boldsymbol{v}_\alpha)\right] - \frac{\partial H^{\mathrm{B}}}{\partial \boldsymbol{r}_i} + f_{i-1,i}^{\mathrm{tension}} \frac{\boldsymbol{r}_{i-1} - \boldsymbol{r}_i}{|\boldsymbol{r}_{i-1} - \boldsymbol{r}_i|} + \boldsymbol{f}_i^{\mathbf{x}} + \boldsymbol{f}_i^{\mathbf{mb}} + \boldsymbol{f}_i^{\mathbf{visc}}(\boldsymbol{v}_i) = 0, \\ \qquad\qquad \text{for actin subunit } i \text{ at the pointed end} \\ \displaystyle\sum_i \left[-\boldsymbol{f}_{i,\alpha}^{\mathbf{cap}} - \boldsymbol{f}_{i,\alpha}^{\mathbf{pull}}(\boldsymbol{v}_i, \boldsymbol{v}_\alpha)\right] + \boldsymbol{f}_{\boldsymbol{\alpha}}^{\mathbf{excl}} + \boldsymbol{f}_{\boldsymbol{\alpha}}^{\mathbf{mb}} + f_\alpha^{\mathrm{anch}}(\boldsymbol{r}_\alpha)\hat{\boldsymbol{r}} + \boldsymbol{f}_{\mathbf{myo}}^{\mathbf{drag,mb}}(\boldsymbol{v}_\alpha) + \boldsymbol{f}_{\boldsymbol{\alpha}}^{\mathbf{diff}} = 0, \ \text{for anchored myosin cluster } \alpha \end{cases}$$

and the constraint equations

$$\frac{dg_i}{dt} = \frac{\partial g_i}{\partial t} + \frac{\partial g_i}{\partial x_j}\frac{dx_j}{dt} = -\frac{1}{\tau} g_i, \quad \text{for myosins, formins, and actin subunits}$$

for the unknown variables $\{\boldsymbol{v}_i\}$, $\{\boldsymbol{v}_{\boldsymbol{\alpha}}\}$, and the Lagrange multipliers $\{f_{i,i+1}^{\text{tension}}\}$, $\{f_i^{\text{anch}}\}$ and $\{f_\alpha^{\text{anch}}\}$ for each ring component. The constraints $\{g_i(\{x_j\}) = 0\}$ represent the anchoring of formins and myosins to the membrane, and the maintenance of distance between neighboring actin subunits (see subsection 1.3). The Euler method with a time step $\Delta t = 0.01$ s and $\tau = 10\Delta t$ is used to evolve the system. The scheme was adapted from Witkin et al. (57). At each time step, components are added to and removed from the simulation according to turnover dynamics.

To optimize simulation running time and enable larger timesteps, we added a pairwise drag force $\boldsymbol{f} = -\gamma_{\text{a}}\boldsymbol{\Delta v}$ between every pair of neighboring actin subunits and between an actin subunit and its bound myosin cluster, in order to suppress spurious oscillations. Here, $\boldsymbol{\Delta v}$ is the relative velocity in each pair and the artificial drag coefficient $\gamma_{\text{a}} = 4$ pN $\cdot$ s/μm. No net force was added to the simulation as this is a pairwise interaction.

5. Three-Dimensional Molecularly Explicit Model of the Cytokinetic Ring in Permeabilized *S. japonicus* Protoplasts (Ghosts). We adapted the model of the normal contractile ring to describe the ring in ghost cells, permeabilized *S. japonicus* protoplasts. Initially, following ATP addition, formin and actin filaments are present in these ghost cell rings, and both components remain present as time progresses (28). We assume the actin cross-linker α-actinin is also initially present in these rings (however, α-actinin rapidly dissociates, so its initial presence had essentially no influence on our simulation results.) In ghost cells, ring components no longer bind to the ring, and unbinding dynamics are slowed down. The fraction of actin in the ring in permeabilized protoplasts does not decrease with time upon treatment with ATP and phallacidin (28). This implies that formin (bound to the barbed end of actin filaments) unbinds the ring with negligible rate, $k_{\text{off,ghost}}^{\text{for}} = 0$. We tuned the cofilin-mediated severing rate $r_{\text{sev,ghost}}$ in permeabilized protoplasts to reproduce the fraction of actin remaining in the ring at 40 min after treatment with ATP alone (*SI Appendix*, Table S1). Actin polymerization is absent, $v_{\text{pol}} = 0$. We tuned the myosin II cluster off rate $k_{\text{off}}^{\text{myo}}$ to be consistent with our measurements of the time course of Rlc1-GFP intensity (*SI Appendix*, Fig. S3*A*). Here, we have interpreted the decrease in myosin II intensity over time as due to myosin II loss from the ring. However, we found that myosin II aggregation kinetics were qualitatively unchanged even when we assumed there was no myosin II loss whatsoever, by setting $k_{\text{off}}^{\text{myo}}$ to zero in five simulated runs, snapshots from one of which are shown in *SI Appendix*, Fig. S3*B*. (In this interpretation, the decrease in Rlc1-GFP intensity of *SI Appendix*, Fig. S3*A* would be attributed to photobleaching.) Cross-linker binding rates are set to zero to reflect an absence of cross-linker association to the ring in cell ghosts. For the rings of Fig. 5, along with cross-linker turnover, either actin or myosin turnover processes were abolished as indicated. To simulate cell ghost rings with blebbistatin, *SI Appendix*, Fig. S6, in addition to abolishing turnover we switched off forces exerted on actin filaments by a subset of myosin clusters whose identity was refreshed every second.

6. Image Analysis. We analyzed 3D confocal micrographs of rings in cell ghosts in Fiji (58). After isolating a 3D volume containing the ring, we identified a best-fit plane where the maximum amount of Rlc1-GFP fluorescence was present. We then rotated the image such that the *z* axis of the rotated 3D image is parallel to the normal to the best-fit plane and performed a sum intensity projection to get a two-dimensional image. We performed background subtraction using the rolling ball technique with a radius of 50 pixels. We measured the total fluorescence in a rectangular region containing the ring (*SI Appendix*, Fig. S3*A*). We used contours of finite thickness coincident with the ring to generate kymographs using the "max" option in the Kymograph plugin developed by Seitz and Surrey (59). Kymographs were analyzed in MATLAB. Aggregates were identified as peaks in the intensity at each time instant in kymographs. We only indicated aggregation events in Figs. 2*A* and 3*C* which were flagged by the algorithm, with the exception of the third red asterisk from the left in Fig. 3*C* which we judged to be a valid aggregation event despite not being flagged by the algorithm. Brightness and contrast of each entire image was adjusted for presentation purposes in Figs. 1*C* and 2*A* and *SI Appendix*, Fig. S6*A*. In *SI Appendix*, Fig. S6*A* we performed maximum intensity projection along the *z* axis without 3D rotation and additionally corrected for drift in the X–Y plane. We detected gaps by eye in *SI Appendix*, Fig. S6 and then measured gap size in Fiji.

Images of simulations were generated by convolving myosin positions with a Gaussian with a full-width half-maximum of 600 nm to mimic the experimental microscope point spread function (PSF). Rings in our experimental images are oriented arbitrarily in 3D space and thus are affected by the small PSF width in the X–Y plane and the comparatively larger PSF widths in the X–Z and Y–Z planes.

7. Variation of Parameters in the Turnover Scans of *SI Appendix*, Fig. S5. We varied myosin and actin turnover times in the runs of *SI Appendix*, Fig. S5. For myosin turnover, we varied the off-rate constant $k_{\text{off}}^{\text{myo}}$ so that the lifetime of myosin clusters is variable. At each ring location we chose the on-rate constant such that the ratio of on- and off-rate constants had the value we used in simulations of normal rings, where the ratio was chosen to generate the nonuniform myosin density profile observed experimentally, with its ~ 1-μm correlation length (see subsection 4.4). We varied the off-rate constant $k_{\text{off}}^{\text{for}}$ of formin dimers while maintaining the ratio of on- and off-rate constants to preserve mean formin density and thus the total number of filaments. To preserve filament length statistics, we also simultaneously varied the rate of filament growth v_{pol} and severing r_{sev} such that the ratios $k_{\text{off}}^{\text{for}}/v_{\text{pol}}$ and $r_{\text{sev}}/v_{\text{pol}}$ remain fixed. Steady-state filament length distributions depend only on these ratios (see next paragraph). We set the load-free velocity of myosin v_{myo}^0 to five times the normal value to enable comparison of simulations with different actin turnover times with minimal complications caused by the different values of v_{pol} (a change in v_{pol} changes the forces that myosin exerts on growing actin filaments, according to the myosin force-velocity relation). Initial conditions were randomly generated rings, as described in subsection 4.5.

7.1 Derivation of the steady-state filament length distribution. Let $p(l)$ denote the steady-state probability distribution of filament lengths l. During a small time interval such that a filament grows a small amount Δl, the processes that alter $p(l)$ are growth of filaments whose length was $l - \Delta l$, growth of filaments whose length was l, and severing of filaments with lengths larger than l. In steady state, there is no net change in the distribution. To order Δl, the change of $p(l)$ in this small time interval is

$$\Delta p(l) = p(l - \Delta l)\left(1 - \frac{k_{\text{off}}^{\text{for}}\Delta l}{v_{\text{pol}}} - \frac{r_{\text{sev}} l \Delta l}{v_{\text{pol}}}\right) - p(l) + \sum_{k=1}^{\infty} p(l + k\Delta l)\frac{r_{\text{sev}}(\Delta l)^2}{v_{\text{pol}}} = 0.$$

Subtracting a similar equation for $\Delta p(l - \Delta l)$ from $\Delta p(l)$ and using coefficients of the lowest-order term, in the continuous limit we get

$$\frac{d^2p}{dl^2} + \left(\frac{k_{\text{off}}^{\text{for}}}{v_{\text{pol}}} + \frac{r_{\text{sev}} l}{v_{\text{pol}}}\right)\frac{dp}{dl} + \frac{2r_{\text{sev}}p}{v_{\text{pol}}} = 0.$$

It follows that the length distribution $p(l)$ depends only on the ratios $k_{\text{off}}^{\text{for}}/v_{\text{pol}}$ and $r_{\text{sev}}/v_{\text{pol}}$.

Data, Materials, and Software Availability. Experimental data and simulation results supporting the findings of this paper and codes to perform the simulations, to analyze the data, and to generate the technical figures are available in the Zenodo repositories https://zenodo.org/record/6989129 (60) and https://zenodo.org/record/6639126 (61). The codes are also available in a GitHub repository (https://github.com/sathish-t/myoagg/releases/tag/v1.0.0).

ACKNOWLEDGMENTS. We thank Yutao Li for assistance with image processing, Dong An and Tianyi Zhu for assistance with figures, and Zach McDargh for helpful discussions. This work was supported by the National Institute of General Medical Sciences of the NIH under award number R01GM086731 to B.O. M.K.B. was supported by a senior investigator award from the Wellcome Trust (WT101885MA). The content is solely the responsibility of the authors and does not necessarily represent the official views of the NIH or the Wellcome Trust, UK. We acknowledge computing resources from Columbia University's Shared Research Computing Facility project.

1. M. Glotzer, Cytokinesis in Metazoa and Fungi. *Cold Spring Harb. Perspect. Biol.* **9**, a022343 (2017).
2. T. D. Pollard, B. O'Shaughnessy, Molecular mechanism of cytokinesis. *Annu. Rev. Biochem.* **88**, 661–689 (2019).
3. S. Thiyagarajan, E. L. Munteanu, R. Arasada, T. D. Pollard, B. O'Shaughnessy, The fission yeast cytokinetic contractile ring regulates septum shape and closure. *J Cell Sci*. **128**, 3672–3681 (2015).
4. E. Munro, J. Nance, J. R. Priess, Cortical flows powered by asymmetrical contraction transport PAR proteins to establish and maintain anterior-posterior polarity in the early *C. elegans* embryo. *Dev. Cell* **7**, 413–424 (2004).
5. J. Renkawitz, M. Sixt, Mechanisms of force generation and force transmission during interstitial leukocyte migration. *EMBO Rep.* **11**, 744–750 (2010).
6. A. C. Martin, M. Kaschube, E. F. Wieschaus, Pulsed contractions of an actin-myosin network drive apical constriction. *Nature* **457**, 495–499 (2009).
7. M. Roh-Johnson *et al.*, Triggering a cell shape change by exploiting preexisting actomyosin contractions. *Science* **335**, 1232–1235 (2012).
8. T. Nishimura, H. Honda, M. Takeichi, Planar cell polarity links axes of spatial dynamics in neural-tube closure. *Cell* **149**, 1084–1097 (2012).
9. M. A. Smith *et al.*, A zyxin-mediated mechanism for actin stress fiber maintenance and repair. *Dev. Cell* **19**, 365–376 (2010).
10. M. R. Stachowiak *et al.*, A mechanical-biochemical feedback loop regulates remodeling in the actin cytoskeleton. *Proc. Natl. Acad. Sci. U.S.A.* **111**, 17528–17533 (2014).
11. M. R. Stachowiak *et al.*, Self-organization of myosin II in reconstituted actomyosin bundles. *Biophys. J.* **103**, 1265–1274 (2012).
12. M. R. Stachowiak *et al.*, Mechanism of cytokinetic contractile ring constriction in fission yeast. *Dev. Cell* **29**, 547–561 (2014).
13. S. Thiyagarajan, S. Wang, B. O'Shaughnessy, A node organization in the actomyosin contractile ring generates tension and aids stability. *Mol. Biol. Cell* **28**, 3286–3297 (2017).
14. R. Alonso-Matilla, S. Thiyagarajan, B. O'Shaughnessy, Sliding filament and fixed filament mechanisms contribute to ring tension in the cytokinetic contractile ring. *Cytoskeleton (Hoboken)* **76**, 611–625 (2019).
15. J. S. Bois, F. Jülicher, S. W. Grill, Pattern formation in active fluids. *Phys. Rev. Lett.* **106**, 028103 (2011).
16. M. Nishikawa, S. R. Naganathan, F. Julicher, S. W. Grill, Controlling contractile instabilities in the actomyosin cortex. *eLife* **6**, e19595 (2017).
17. V. Wollrab, R. Thiagarajan, A. Wald, K. Kruse, D. Riveline, Still and rotating myosin clusters determine cytokinetic ring constriction. *Nat. Commun.* **7**, 11860 (2016).
18. C. Laplante *et al.*, Three myosins contribute uniquely to the assembly and constriction of the fission yeast cytokinetic contractile ring. *Curr. Biol.* **25**, 1955–1965 (2015).
19. A. C. Reymann, F. Staniscia, A. Erzberger, G. Salbreux, S. W. Grill, Cortical flow aligns actin filaments to form a furrow. *eLife* **5**, 17807 (2016).
20. S. C. Wang *et al.*, Cortical forces and CDC-42 control clustering of PAR proteins for *Caenorhabditis elegans* embryonic polarization. *Nat. Cell Biol.* **19**, 988–995 (2017).
21. M. A. Baird *et al.*, Local pulsatile contractions are an intrinsic property of the myosin 2A motor in the cortical cytoskeleton of adherent cells. *Mol. Biol. Cell* **28**, 240–251 (2017).
22. H. Y. Kim, L. A. Davidson, Punctuated actin contractions during convergent extension and their permissive regulation by the non-canonical Wnt-signaling pathway. *J. Cell Sci.* **124**, 635–646 (2011).
23. X. Qin *et al.*, A biochemical network controlling basal myosin oscillation. *Nat. Commun.* **9**, 1210 (2018).
24. A. Kamnev *et al.*, Time-varying mobility and turnover of actomyosin ring components during cytokinesis in *Schizosaccharomyces pombe*. *Mol. Biol. Cell* **32**, 237–246 (2020).
25. M. Fritzsche, A. Lewalle, T. Duke, K. Kruse, G. Charras, Analysis of turnover dynamics of the submembranous actin cortex. *Mol. Biol. Cell* **24**, 757–767 (2013).
26. E. Hannezo, B. Dong, P. Recho, J. F. Joanny, S. Hayashi, Cortical instability drives periodic supracellular actin pattern formation in epithelial tubes. *Proc. Natl. Acad. Sci. U.S.A.* **112**, 8620–8625 (2015).
27. M. Mishra *et al.*, In vitro contraction of cytokinetic ring depends on myosin II but not on actin dynamics. *Nat. Cell Biol.* **15**, 853–859 (2013).
28. T. G. Chew *et al.*, Actin turnover maintains actin filament homeostasis during cytokinetic ring contraction. *J. Cell Biol.* **216**, 2657–2667 (2017).
29. T. E. Sladewski, M. J. Previs, M. Lord, Regulation of fission yeast myosin-II function and contractile ring dynamics by regulatory light-chain and heavy-chain phosphorylation. *Mol. Biol. Cell* **20**, 3941–3952 (2009).
30. M. Takaine, O. Numata, K. Nakano, An actin-myosin-II interaction is involved in maintaining the contractile ring in fission yeast. *J. Cell Sci.* **128**, 2903–2918 (2015).
31. S. Wang, B. O'Shaughnessy, Anchoring of actin to the plasma membrane enables tension production in the fission yeast cytokinetic ring. *Mol. Biol. Cell* **30**, 2053–2064 (2019).
32. B. C. Stark, T. E. Sladewski, L. W. Pollard, M. Lord, Tropomyosin and myosin-II cellular levels promote actomyosin ring assembly in fission yeast. *Mol. Biol. Cell* **21**, 989–1000 (2010).
33. C. Laplante, F. Huang, I. R. Tebbs, J. Bewersdorf, T. D. Pollard, Molecular organization of cytokinesis nodes and contractile rings by super-resolution fluorescence microscopy of live fission yeast. *Proc. Natl. Acad. Sci. U.S.A.* **113**, E5876–E5885 (2016).
34. R. J. Pelham, F. Chang, Actin dynamics in the contractile ring during cytokinesis in fission yeast. *Nature* **419**, 82–86 (2002).
35. J. Q. Wu, T. D. Pollard, Counting cytokinesis proteins globally and locally in fission yeast. *Science* **310**, 310–314 (2005).
36. N. Courtemanche, T. D. Pollard, Q. Chen, Avoiding artefacts when counting polymerized actin in live cells with LifeAct fused to fluorescent proteins. *Nat. Cell Biol.* **18**, 676–683 (2016).
37. J. Limouze, A. F. Straight, T. Mitchison, J. R. Sellers, Specificity of blebbistatin, an inhibitor of myosin II. *J. Muscle Res. Cell Motil.* **25**, 337–341 (2004).
38. M. Kovács, J. Tóth, C. Hetényi, A. Málnási-Csizmadia, J. R. Sellers, Mechanism of blebbistatin inhibition of myosin II. *J. Biol. Chem.* **279**, 35557–35563 (2004).
39. D. Vavylonis, J. Q. Wu, S. Hao, B. O'Shaughnessy, T. D. Pollard, Assembly mechanism of the contractile ring for cytokinesis by fission yeast. *Science* **319**, 97–100 (2008).
40. N. Maximova, O. Dahl, Environmental implications of aggregation phenomena: Current understanding. *Curr. Opin. Colloid Interface Sci.* **11**, 246–266 (2006).
41. P. Meakin, Fractal aggregates. *Adv. Colloid Interface Sci.* **28**, 249–331 (1988).
42. K. Takiguchi, Heavy meromyosin induces sliding movements between antiparallel actin filaments. *J. Biochem.* **109**, 520–527 (1991).
43. Q. Chen, T. D. Pollard, Actin filament severing by cofilin is more important for assembly than constriction of the cytokinetic contractile ring. *J. Cell Biol.* **195**, 485–498 (2011).
44. T. H. Cheffings, N. J. Burroughs, M. K. Balasubramanian, Actin turnover ensures uniform tension distribution during cytokinetic actomyosin ring contraction. *Mol. Biol. Cell* **30**, 933–941 (2019).
45. M. Malla, T. D. Pollard, Q. Chen, Counting actin in contractile rings reveals novel contributions of cofilin and type II myosins to fission yeast cytokinesis. *Mol. Biol. Cell* **33**, ar51 (2022).
46. Z. McDargh, T. Zhu, H. Zhu, B. O'Shaughnessy, Actin turnover protects the cytokinetic contractile ring from structural instability. *J Cell Sci.* **136**, jcs259969 (2023).
47. J. R. Sellers, S. M. Heissler, Nonmuscle myosin-2 isoforms. *Curr. Biol.* **29**, R275–R278 (2019).
48. J. Huang *et al.*, Curvature-induced expulsion of actomyosin bundles during cytokinetic ring contraction. *eLife* **5**, 21383 (2016).
49. J. Huang, M. Mishra, S. Palani, T. G. Chew, M. K. Balasubramanian, Isolation of cytokinetic actomyosin rings from *Saccharomyces cerevisiae* and *Schizosaccharomyces pombe*. *Methods Mol. Biol.* **1369**, 125–136 (2016).
50. I. Flor-Parra, M. Bernal, J. Zhurinsky, R. R. Daga, Cell migration and division in amoeboid-like fission yeast. *Biol. Open* **3**, 108–115 (2014).
51. A. Ott, M. Magnasco, A. Simon, A. Libchaber, Measurement of the persistence length of polymerized actin using fluorescence microscopy. *Phys. Rev. E* **48**, R1642–R1645 (1993).
52. D. Riveline, C. H. Wiggins, R. E. Goldstein, A. Ott, Elastohydrodynamic study of actin filaments using fluorescence microscopy. *Phys. Rev. E* **56**, R1330–R1333 (1997).
53. D. Laporte, V. C. Coffman, I. J. Lee, J. Q. Wu, Assembly and architecture of precursor nodes during fission yeast cytokinesis. *J. Cell Biol.* **192**, 1005–1021 (2011).
54. E. Gauger, H. Stark, Numerical study of a microscopic artificial swimmer. *Phys. Rev. E* **74**, 021907 (2006).
55. T. Kanbe, I. Kobayashi, K. Tanaka, Dynamics of cytoplasmic organelles in the cell cycle of the fission yeast *Schizosaccharomyces pombe*: Three-dimensional reconstruction from serial sections. *J. Cell Sci.* **94**, 647–656 (1989).
56. A. Yonetani *et al.*, Regulation and targeting of the fission yeast formin cdc12p in cytokinesis. *Mol. Biol. Cell* **19**, 2208–2219 (2008).
57. A. Witkin, M. Gleicher, W. Welch, "Interactive dynamics" in *Proceedings of the 1990 Symposium on Interactive 3D Graphics* (ACM, New York, 1990), pp. 11-21.
58. J. Schindelin *et al.*, Fiji: An open-source platform for biological-image analysis. *Nat. Methods* **9**, 676–682 (2012).
59. A. Seitz, T. Surrey, Processive movement of single kinesins on crowded microtubules visualized using quantum dots. *EMBO J.* **25**, 267–277 (2006).
60. S. Thiyagarajan *et al.*, Myosin turnover controls actomyosin contractile instability (Version 3) [Data set]. Zenodo. https://doi.org/10.5281/zenodo.6989129. Deposited 19 September 2022.
61. S. Thiyagarajan, S. Wang, B. O'Shaughnessy, sathish-t/myoagg: Initial release (v1.0.0). Zenodo. https://doi.org/10.5281/zenodo.6639126. Deposited 13 June 2022.